

Ultraviolet and blue photoluminescence from sputter deposited Ge nanocrystals embedded in SiO₂ matrix

P. K. Giri,^{1,a)} S. Bhattacharyya,¹ Satchi Kumari,¹ Kaustuv Das,² S. K. Ray,²
B. K. Panigrahi,³ and K. G. M. Nair³

¹*Department of Physics and Centre for Nanotechnology, Indian Institute of Technology, Guwahati 781039, India*

²*Department of Physics and Meteorology, Indian Institute of Technology, Kharagpur 721302, India*

³*Materials Science Division, Indira Gandhi Center for Atomic Research, Kalpakkam 603102, India*

(Received 8 February 2008; accepted 28 March 2008; published online 28 May 2008)

Ge nanocrystals (NCs) embedded in silicon dioxide (SiO₂) matrix are grown by radio-frequency magnetron sputtering and studied in order to understand the origin of ultraviolet (UV) and blue photoluminescence (PL) from the NC-SiO₂ system. Ge NCs of diameter 7–8 nm are formed after postdeposition annealing, as confirmed by transmission electron microscopy and Raman scattering studies. Optical Raman studies indicate the presence of strain in the embedded Ge NCs. Polarization dependent low frequency Raman studies reveal surface symmetrical and surface quadrupolar acoustic phonon modes of Ge NCs. PL studies with 488 nm excitation shows a broad emission band peaked at ~545 nm, which is attributed to oxygen deficient defects in the SiO₂ matrix. PL studies with 325 nm excitation show additional strong peaks in the 377–400 nm region. Time resolved PL studies in the UV-blue range show double exponential decay dynamics in the nanosecond time scale, irrespective of the NC size. Comparative studies of PL emission from SiO₂ layers with no Ge content and with Ge content show that the ~400 nm PL emission is originated from a defective NC/SiO₂ interface and the band is not unique to the presence of Ge. PL excitation spectroscopy measurements show large Stokes shift for the UV emission bands. We propose that the intense UV peaks at ~377 nm is originated from the twofold coordinated silicon defect at the interface between NC and SiO₂ matrix and it is not necessarily specific to the presence of Ge in the oxide matrix. It is believed that due to the influence of strain on the NCs and interface states, PL from quantum confined carriers may be partially quenched for the embedded Ge NCs. © 2008 American Institute of Physics. [DOI: 10.1063/1.2930877]

I. INTRODUCTION

In recent years, several studies on the optical properties of Ge nanocrystals (NCs) embedded in Si oxide films and on their photoluminescence (PL) mechanism have been reported.^{1–9} Intriguing role of defects and stress on the surface of the NCs and the role of defects in the embedding matrix in the light emission properties are poorly understood for Ge NCs as compared to their counterpart in Si NCs. Despite numerous studies, a specific mechanism for the visible and near-infrared PL from Ge NCs that are commonly prepared either by ion-implantation or sputter deposition method has not been pinpointed. Several studies have indicated that the defects in the surrounding matrix are primarily responsible for broad PL in the visible region,^{1,2,4} while some studies attribute the luminescence to quantum confinement of charge carriers in the NCs.³ Takeoka *et al.*¹⁰ attributed the size dependent near-infrared PL to quantum confinement effect, while Wu *et al.* and Lannoo *et al.* attributed the infrared PL to defect states in the NCs.^{2,11} Ge quantum dots without any embedding matrix grown by pulsed laser deposition have been shown to produce size dependent infrared PL.¹² Near-infrared PL emission at 1350 nm has been attributed to radiative recombination of excitons confined in the

NCs.¹³ It has been reported that near-infrared PL intensity drastically goes down with increasing size of Ge NCs.¹⁴

Recently, violet-blue PL emission has been reported from Ge implanted SiO₂ layers and there exists a controversy regarding the origin of the violet-blue PL.^{15,16} Rebohle *et al.*^{6,17} reported a strong blue-violet PL and electroluminescence from Ge implanted and Si implanted SiO₂ layer and they attributed the observed PL to neutral oxygen vacancies in SiO₂.¹⁰ Similarly, Sahoo *et al.* observed a stable violet emission from Ge implanted α -quartz and attributed it to Ge related defects.⁷ Zacharias and Fauchet⁴ argued that ~400 nm blue luminescence must be related to the formation of Ge or GeO₂ NCs in the oxide matrix and they suggested that defects at the NC/matrix interface is responsible for the emission. On the other hand, Liao *et al.*⁸ and Meinardi and Paleari¹⁸ observed the violet PL in the SiO₂ samples that does not contain Ge atoms and the violet emission was attributed to oxygen deficient defects in SiO₂. Violet luminescence in Ge NCs/Ge oxide structures formed by dry oxidation of polycrystalline SiGe has been attributed to defects at the Ge/GeO₂ interface.¹⁹ Although the UV-violet and blue emissions have been reported from Si and Ge ion-implanted SiO₂ layers,^{17,20} no systematic studies have reported on the UV and violet PL emission from sputter deposited Ge NC.⁴ It may be noted that strong UV PL from silicon oxide films prepared by magnetron sputtering has been

^{a)}Electronic mail: giri@iitg.ernet.in.

reported.²¹ Yang *et al.*²² attributed it to the interface defect, while Du *et al.*²³ attributed it to the quantum confinement effect of Si NCs.

Raman studies have been utilized to monitor stress in Ge NCs embedded in silicon dioxide.^{24,25} However, the implications of stress on the optical properties of NCs are not explored in the literature. Low frequency Raman scattering (LFRS) has proved to be a powerful tool to monitor the size and surface vibrational modes of embedded NCs.²⁶ However, very little is known about the surface phonon modes of Ge NCs prepared by sputter deposition. Recent calculations have shown that embedding matrix has strong influence over the acoustic phonon modes of semiconductor NCs.²⁷

In this work, we study the light emitting and vibrational properties of SiO₂ embedded Ge NCs prepared by sputter deposition and subsequent annealing at different temperatures. Ge NCs embedded in SiO₂ matrix are characterized by x-ray diffraction (XRD), transmission electron microscopy (TEM), Fourier transform infrared (FTIR) spectroscopy, low frequency and optical Raman scattering, steady state and time resolved PL, and PL excitation (PLE) spectroscopy techniques. The steady state PL measurements are carried out using two different excitation laser sources: 325 and 488 nm. The origin of the visible and UV emission at room temperature is explored by careful analysis of samples prepared with and without Ge content in the SiO₂ matrix.

II. EXPERIMENTAL DETAILS

The Ge–SiO₂ thin films were deposited on (100) oriented *p*-type Si substrates by rf magnetron cosputtering. Prior to deposition, the Si substrates were dipped in dilute hydrofluoric acid to remove the surface native oxide followed by rinsing in de-ionized water and drying in a flux of N₂. The target used was a 3 in. *n*-type Si wafer masked with Ge wafer pieces of defined area. The chamber was first evacuated to a base pressure of 1×10^{-6} Torr. The target to substrate distance was kept fixed at 6 cm and the working pressure was maintained at 0.11 Torr by introducing oxygen and argon in the ratio of 2:1. The depositions were carried out at rf powers of 50 W for 1 h. No external heating of the substrate was employed during deposition. Both sputtered Si and Ge species while transporting through the oxygen discharge become oxidized and condensed on the substrate. As-deposited samples are subsequently annealed at 700 °C (Ge1) and 900 °C (Ge2) for 1 h in nitrogen ambient to grow Ge NCs of various sizes. Since Ge is thermodynamically less stable in its oxide form than Si, GeO_x may be reduced to Ge under high temperature annealing. Annealed samples were studied by XRD, TEM, PL, FTIR, and Raman measurements. For comparison, we also prepared a sample (Ar1) where 100 keV Ar⁺ ions were implanted (dose: 5×10^{16} cm⁻²) on a thermally grown SiO₂ layer and subsequently annealed at 900 °C for 1 h in inert gas ambient. Since this implanted sample (Ar1) does not contain any Ge atoms but would certainly contain defects created by ion damage in SiO₂ matrix, we used sample Ar1 for comparison of PL results with samples Ge1 and Ge2. Rutherford back-scattering studies on the annealed Ar1 sample show that the

implanted silicon dioxide layer has a composition of SiO_x ($x=1.8$), i.e., the layer is oxygen deficient. It is well known that ion implantation in SiO₂ causes varieties of defects in SiO₂, such as nonbridging oxygen hole center. Our previous studies on sputter deposited Ge–SiO₂ layer prepared under identical conditions²⁸ show that before postdeposition annealing, Ge nanoclusters are surrounded by SiO_x matrix and with annealing the oxygen content slowly increases in the SiO_x layer.

XRD measurements were performed in grazing incidence mode using a powder diffractometer (Seifert 3003 T/T) in thin film mode. The TEM observations were carried out using a JEM 3000F field emission microscope with an operating voltage of 300 kV. FTIR measurements were performed in a Perkin Elmer made spectrometer (spectrum 1). Raman spectra for all the samples were recorded in the back-scattering geometry using vertically polarized 488 nm argon-ion laser beam, double grating monochromator, and cooled photomultiplier tube. LFRS spectra were recorded from 5 to 40 cm⁻¹ at steps of 0.5 cm⁻¹ using the same setup. Steady state PL measurements were made using two different laser excitations: 325 nm (He–Cd laser) and 488 nm (Ar ion laser). A Jobin-Yvon T64000 spectrometer equipped with a cooled charged coupled detector was used for the UV excitation induced PL measurement. The PL decay measurements were performed using 378 nm excitation pulse of 1.32 ns duration using a commercial fluorescence lifetime setup with a time resolution of 0.113 ns (model IBH Fluorocube). In the PL decay measurement, a cutoff filter was placed before the emission detector to block the light below the wavelength of 385 nm. We also measured emission at a selected wavelength (400 nm) with a monochromator at the emission side. The PLE spectra were recorded using a commercial fluorimeter (Thermo Electron, AB2) with a xenon lamp source and a 350 nm cut on filter.

III. RESULTS AND DISCUSSION

A. Structure and morphology

Figure 1 shows the XRD pattern for the Ge1 and Ge2 samples after postdeposition annealing. Both the samples show the Ge(111) and Ge(311) Bragg peaks at 27.35° and 53.7°, and these peaks are the evidence for Ge NCs present in these samples. The sample Ge1 annealed at 700 °C show the presence of GeO₂ along with small Ge NCs. After annealing at 900 °C, the Ge(111) peak dominates the XRD pattern. The size and distribution of Ge NCs embedded in the oxide matrix were studied using TEM imaging. The inset of Fig. 1 shows a typical TEM image of Ge NCs present in sample Ge2 that was annealed at 900 °C for 1 h. Embedded Ge NCs (dark circular regions) of diameter 7–8 nm are found to be evenly distributed in SiO_x matrix and sizes are apparently uniform with nearly spherical shape. In Ge1, the average size of Ge NCs is expected to be smaller due to the lower temperature of annealing. The sizes of the small NCs are calculated from the LFRS data (discussed later) and in some cases compared to the TEM analysis.

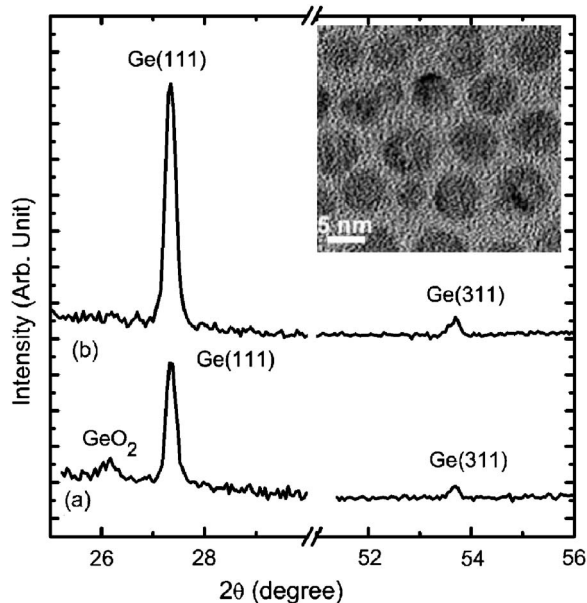


FIG. 1. XRD pattern for Ge1 and Ge2 samples showing Ge(111) and Ge(311) Bragg peaks for NCs. The low temperature annealed Ge1 sample shows GeO₂ peak as well. The inset shows a typical TEM image of Ge2. Spherical Ge NCs (dark circular regions) of diameter 7–8 nm are clearly seen in the SiO₂ matrix (background).

B. Optical Raman scattering

First order Raman spectrum provides a fast and convenient method to determine whether the semiconductor phase is amorphous or crystalline. Typical Raman spectrum from Ge2 is shown in Fig. 2 that shows distinct peaks at 300.9 cm⁻¹, 420 cm⁻¹, and 520 cm⁻¹, which correspond to

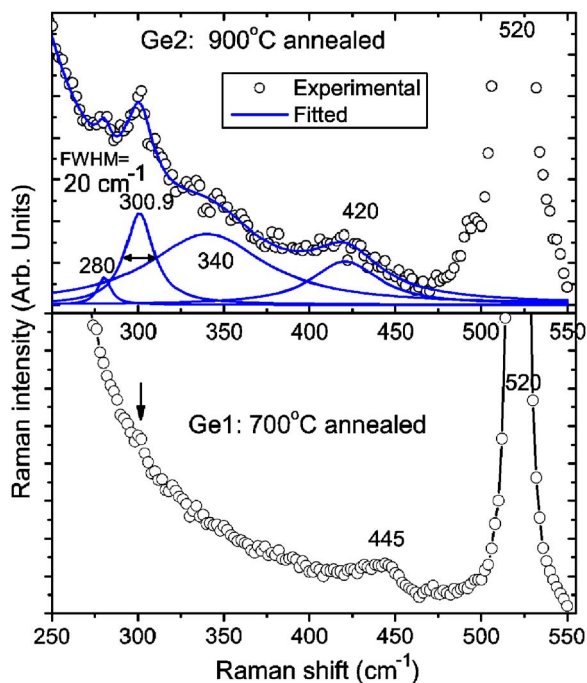


FIG. 2. (Color online) Optical Raman spectra for Ge1 and Ge2, showing Ge–Ge and Si phonon modes. The experimental data (symbols) are fitted with Lorentzian line shapes for constituent peaks. Peak at 300.9 cm⁻¹ shows a FWHM of ~20 cm⁻¹. Due to the small size of Ge NCs in Ge1, Ge related peak at ~300 cm⁻¹ is very weak and marked with an arrow.

scattering from optical phonons involving Ge–Ge, localized Si–Si motion in the neighborhood of one or more Ge atoms in the SiO₂ matrix, and Si–Si vibration modes, respectively.²⁹ Other weak peaks at ~280 and ~340 cm⁻¹ are signatures of Ge related components in the sample. Ge1 sample shows a very weak signature (marked with an arrow at ~300 cm⁻¹) of Ge NCs due to its small size and a distinct peak at ~440 cm⁻¹, which corresponds to the Si–Si vibration in the neighborhood of one or more Ge atoms. For the Ge2 sample spectrum, the full width at half maximum (FWHM) of ~20 cm⁻¹ for the 300.9 cm⁻¹ peak (shown in Fig. 2) is in contrast to the bulk Ge Raman mode at $\omega_{\text{TO-LO}} = 300.4$ cm⁻¹ and FWHM=4.0 cm⁻¹ at room temperature, which indicates the presence of Ge nanocrystallites. The linewidth broadening is primarily caused by confinement of phonons in the Ge NCs. The Raman linewidth is known to be inversely proportional to the size of the NCs.

In order to quantitatively describe the Raman spectra, the standard phonon confinement model³⁰ can be adopted to estimate the mean size d of Ge NCs. For spherical NCs (as found in our samples), the first order Raman spectrum $I(\omega)$ is

$$I(\omega) \propto \int \exp(-q^2 d^2/4) d^3 q / \{ [\omega_0 - \omega(q)]^2 + (\Gamma/2)^2 \}, \quad (1)$$

where $\omega_0 = 300.4$ cm⁻¹; q is expressed in units of $2\pi/a_{\text{Ge}}$, with $a_{\text{Ge}} = 0.565$ nm being the lattice constant of Ge. Γ is the natural linewidth (≈ 3.5 cm⁻¹) and $\omega(q)$ is the dispersion relation for optical phonons in c -Ge. Since the crystallite size d is larger than the lattice constant a_{Ge} , we may take $\omega(q) = [A + B \cos(\pi q/2)]^{1/2}$, where $A = 1.578 \times 10^5$ cm⁻² and $B = 1.000 \times 10^5$ cm⁻².²⁴ Using the above equation, we calculate the Raman intensity profile to obtain the mean crystallite size. Note that we expect a downshift of the Raman peak position due to the small crystallite size, which is contrary to the observation of small upshift (~ 0.5 cm⁻¹) of the peak. In the Raman spectra of Ge2 sample, the observed FWHM of 20 cm⁻¹ for the 300.9 cm⁻¹ peak would correspond to an average NC size of $d = 4.6$ nm, as predicted from Eq. (1). However, the mean size of the NCs as determined from TEM and LFRS studies (shown later) are about double of this size. Equation (1) predicts that a crystallite size of 7–8 nm would give rise to a FWHM of 9–11 cm⁻¹, in contrast to the observed FWHM of 20 cm⁻¹. Hence, the additional linewidth and the observed upshift of 300.4 cm⁻¹ peak must be contributed by other factors such as strain in these small crystallites. The compressive stress exerted on Ge NCs may increase with decreasing crystallite size,²⁴ because the Ge NCs are embedded in the SiO₂ matrix.

The nearest neighbor distance in a -SiO₂ is of the order of 0.16 nm and that in Ge crystals is 0.24 nm. The mismatch will result in a compressive stress on the Ge NCs. The stress causes upward shift of the c -Ge peak thereby compensating the downward shift caused by the confinement on phonon frequency. According to the calculation of Wu *et al.*,²⁴ for NC size of 7–8 nm, we expect a downshift of Raman peak frequency by ~ 3 cm⁻¹. The compressive stress s can be estimated from this downshift ($\Delta\omega$) using a formula $\Delta\omega = -s(P + 2Q)/2\omega_c$, where $P = -1.3\omega_c^2$ and $Q = -1.65\omega_c^2$ are the phonon deformation potentials of Ge, and ω_c is the fre-

quency of Ge crystalline peak.²⁴ Since our TEM studies do not show any significant distribution in the NC sizes, we neglect the contribution of particle size distribution to Raman line shape and estimate a compressive stress of 0.34% for the Ge NCs present in sample Ge2. Though this is an upper estimate of the stress, the stress is primarily responsible for the upshift of Raman peak and the additional broadening in linewidth of Raman spectra. In sample Ge1, the compressive stress would be relatively large since the NC sizes are expected to be smaller; as a result, the Raman signal is too weak. The broad Raman spectra from sputter deposited Ge have been reported by Das *et al.*²⁸ and have been attributed to the size distribution and the strain in the deposited film without any quantitative analysis. Our results are consistent with the previous reports on strain in the SiO₂-embedded Ge NCs.^{25,31} There could be various sources of strain in embedded Ge NCs: (i) Liquid-solid phase transition in Ge during high temperature heat treatment; (ii) lattice mismatch between Ge and SiO₂ matrix, and lattice mismatch between Si and Ge; (iii) composition of the surrounding oxide matrix such as silicon suboxide (SiO_x) or Ge suboxides (GeO_x); and (iv) imperfect surface reconstruction during growth of NCs. Using Rutherford backscattering spectrometry, we have found that in ion-implanted samples, the surrounding matrix of NCs has a composition of SiO_x ($x \approx 1.8$). Similarly, the compositions of GeO_x and SiO_x are sensitive to the processing temperature and partial pressure of oxygen during sputter deposition. In fact, our Raman results show that for Ge1 sample the Si-Ge peak is at 440 cm⁻¹, whereas in Ge2 sample the Si-Ge peak is located at 420 cm⁻¹. This indicates that in Ge2 sample, some of the Si-Si motions are replaced by Si-Ge bonds²⁹ as a result of higher temperature annealing, as compared to the Ge1 sample. Lopes *et al.*³² found that in Ge implanted SiO₂, even after 900 °C annealing, a significant fraction of up to ~20% of the Ge content still remains distributed in the oxide matrix around the NCs. Hence, these factors contribute to the strain and the present Raman results confirm the presence of strain in Ge NCs.

C. Low frequency Raman scattering

LFRS is a powerful technique to study the confined acoustic phonon modes in NCs and to find the crystallite size from the measurement of low frequency phonon modes. LFRS peak frequencies are inversely proportional to the size of the NCs.²⁶ As shown in Fig. 3, in Ge2 sample, the LFRS peak is very close to the Rayleigh tail, whereas in Ge1 two distinct peaks are observed. Figure 3 shows the LFRS spectra for Ge1 and Ge2 samples recorded under VH polarization geometry (vertically polarized incident ray and horizontally polarized scattered rays). In both samples, two distinct peaks are observed. It has been shown that spheroidal modes with $l=0,2$ are Raman active and torsional modes are Raman inactive.^{26,33} In the present study, we assign the lower frequency mode in Fig. 3(a) to surface symmetrical (0,0) mode and the higher frequency mode to surface quadrupolar (0,2) modes of confined acoustic phonons, as per the standard notations for denoting acoustic phonon modes.²⁶ In Ge2

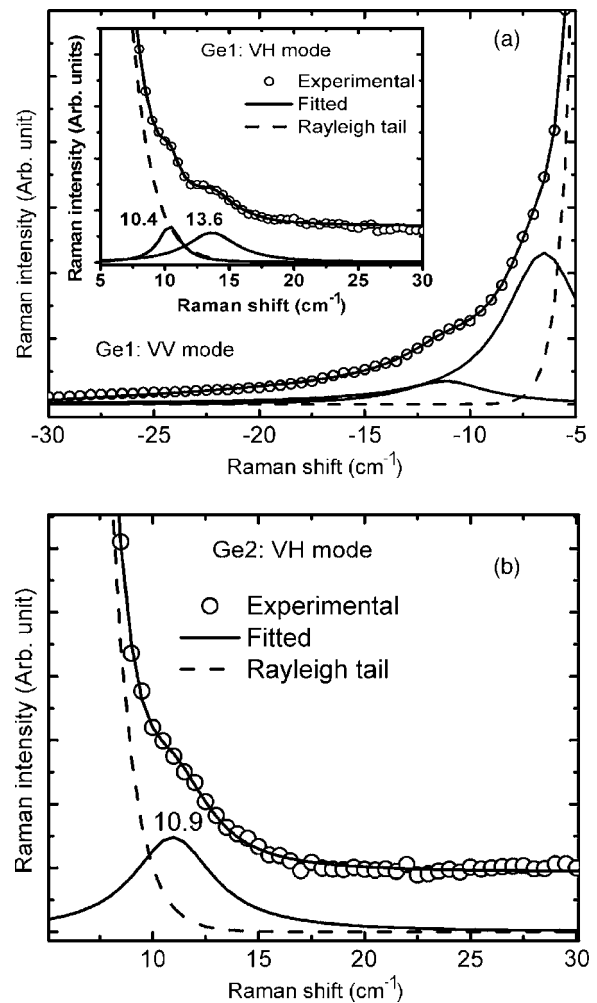


FIG. 3. LFRS spectra of (a) Ge1 and (b) Ge2 samples. Ge1 sample shows two distinct peaks in both VV mode and VH mode [shown as inset in (a)]. Ge2 shows peak at lower frequency due to the presence of larger size NCs. The symbols are the experimental data, the solid lines are the fits with Lorentzian line shape, and the dashed line is the Rayleigh tail. The peak positions are denoted in cm⁻¹ unit.

sample, only one peak could be measured, as shown in Fig. 3(b), since the lower frequency peak is merged with the Rayleigh tail as expected for larger NC size. Thus, the observed mode in Ge2 is assigned to (0,2) surface quadrupolar mode. From the measured low frequency modes in Ge1, the NC sizes are calculated as 7.3 nm using the standard formula for spheroidal mode in Ge NCs:³⁴ $\nu_0^S = 0.7v_t/dc$ ($n=0$), where c is the velocity of light, d is the average diameter of the NCs, and v_t is the transverse velocity of sound in Ge NCs. We have assumed a $v_t = 3.25 \times 10^5$ cm/s for Ge. In Ge2 sample, the corresponding sizes grow to 9.1 nm as calculated from the LFRS peak position. The sizes estimated from LFRS are quite consistent with the sizes measured from the TEM analysis. Any deviation in the results would be expected for nonspherical shapes of the NCs and assumption of appropriate boundary conditions.²⁷

Figure 4 shows the LFRS spectra from the Ar implanted SiO₂ layer that was annealed at 900 °C. Both the Stokes and anti-Stokes Raman spectra show distinct low frequency phonon modes that are signatures of nanocluster or NC formation.²⁶ Ion implantation and subsequent annealing are

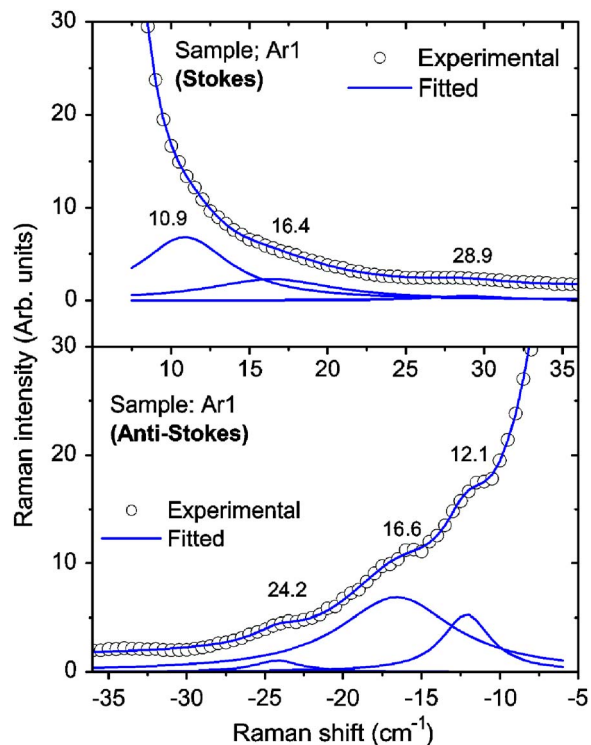


FIG. 4. (Color online) Stokes and anti-Stokes LFRS spectra for Ar1 sample showing signature of Si nanocluster in the SiO_2 matrix.

believed to create Si nanoclusters in the SiO_2 matrix. The mechanism of forming Si nanoclusters in Ar implanted SiO_2 may be as follows: During implantation, the energetic Ar ions cause displacement of Si atoms in the Si rich oxide (SiO_x), which can aggregate and form nanoclusters or NCs of Si during thermal annealing. It has been reported that at high fluence, Ge ion implantation in SiO_2 followed by heat treatment at 900°C produces embedded Si NCs, in addition to Ge NCs.³⁵ In the present case, the sizes of the Si nanoclusters are likely to be very small since excess Si concentration may not be locally high and optical Raman studies on this sample do not show any detectable signal for Si NCs, perhaps due to the ultrasmall size. It has been suggested that Lamb's theory is not applicable for ultrasmall NCs to determine size from the observed low frequency modes. Further, due to the large anisotropy of elastic constant and the matrix effect, a proper estimation of size of Si NCs embedded in SiO_2 matrix is often difficult.³⁶ Hence, quantitative evaluation of Si NC size in Ar1 sample is not attempted. However, the presence of nanoclusters in SiO_2 has important bearing on the PL emission from this sample.

D. Infrared absorption

In order to evaluate the structure of SiO_2 films in sputter deposited oxide and the Ar implanted oxide (thermally grown), we performed normal incidence infrared absorption measurements in the annealed samples. Figure 5 shows the FTIR spectra for samples Ar1, Ge1, and Ge2. We focus on the absorption bands in the region of $800\text{--}1200\text{ cm}^{-1}$ that are related to the quality of the SiO_2 matrix. The band centered at 813 cm^{-1} originates from the symmetrical stretching

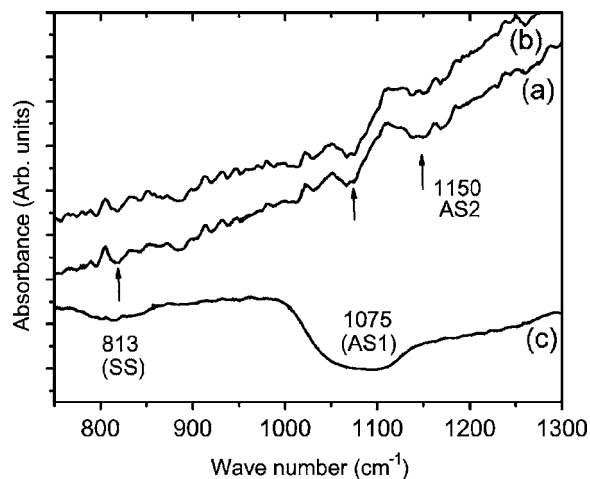


FIG. 5. FTIR spectra for (a) Ge1, (b) Ge2, and (c) Ar1 samples. Peaks related to SS, AS1, and AS2 modes of Si–O–Si linkage are shown with arrows and corresponding wave number in cm^{-1} unit.

(SS) oscillation of the Si–O–Si linkage.³⁷ The strong band centered at about 1075 cm^{-1} is due to the asymmetrical stretching (AS) vibration of the oxygen atom in the Si–O–Si unit, while the other two Si atoms vibrate in phase with each other (AS1 mode).³⁷ The higher frequency shoulder in the region of $\sim 1150\text{--}1200\text{ cm}^{-1}$ originates from the AS oscillation where the two Si atoms adjacent to the oxygen atom oscillate out of phase (AS2 mode). It is evident that AS1 and AS2 modes are relatively strong and very broad in the implanted sample (Ar1) as compared to the sputter deposited sample. Thus, the quality of the Si oxide is widely different in the samples prepared by two different methods. It has been reported that in the sputter deposited $a\text{-SiO}_2\text{:Ge}$ layer, the recovery of the amorphous oxide network and the annealing of the dangling bond defects primarily occur within $500\text{--}700^\circ\text{C}$ and no further significant recovery occurs upon annealing at temperatures above 700°C .³⁷ On the other hand, in the implanted SiO_2 layer, the recovery of the amorphous oxide network is not complete as evidenced by the intense and broad absorption band (AS1) in Fig. 5. In a strongly deformed and less dense $a\text{-SiO}_2$, the AS1 peak is broadened and appears at lower wave number as a result of lower average angle of Si–O–Si bonds. Thus, our results show that the quality of Si oxide matrix in sputter deposited layer is superior to the thermally grown and implanted oxide. Note that all the samples contain Si or Ge nanoclusters embedded in the oxide matrix and thus the SiO_2 network is expected to be distorted to different degrees in different samples.

E. Steady state PL

Figure 6 shows the room temperature PL spectra from Ge1, Ge2, and Ar1 samples. In the visible range, all three samples show a broad peak centered at $\sim 545\text{ nm}$ (2.28 eV) with identical intensity, irrespective of the annealing temperature and preparation method. Since the PL emission from the core of Ge NCs is expected to show size dependence, the observed peak is unlikely to be related to emission from

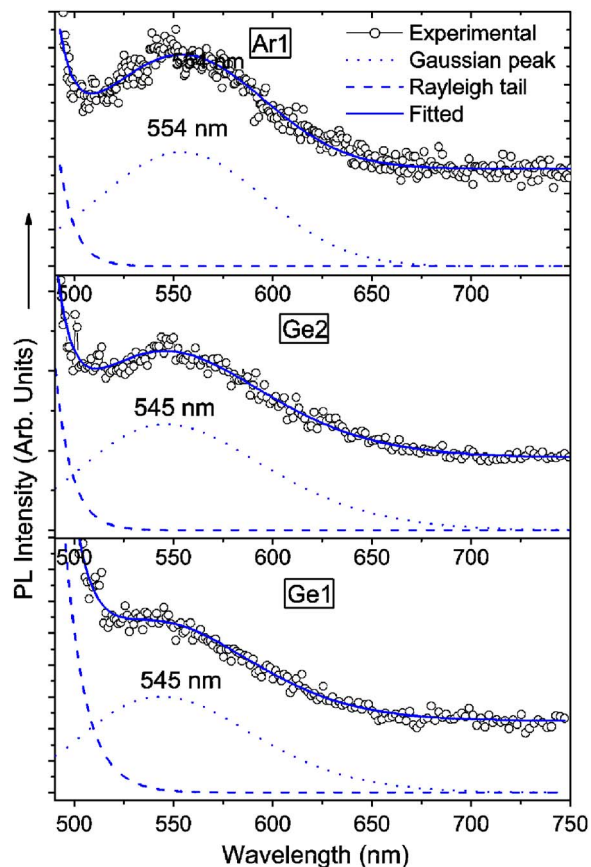


FIG. 6. (Color online) PL spectra of Ar1, Ge1, and Ge2 obtained with 488 nm excitation. A single broad peak (~ 545 nm) with Gaussian line shape fits the experimental data in all cases.

NCs. Further, the peak features are identical for samples with or without Ge atoms. Thus, the peak cannot be related to Ge related defects as well. It may be noted that we observe a very low intensity of visible PL from our samples as compared to the intense PL reported earlier from similarly prepared samples.^{28,38} The size independent visible PL emission from such samples has been commonly attributed to defects in the embedding oxide matrix.

To clarify further on the origin of the visible PL, we studied the PL emission with 325 nm excitation from samples Ge1, Ge2, and Ar1. Figure 7 shows that a broad peak at about ~ 500 nm is common to all samples and additional intense peaks at lower wavelengths (UV-violet region) are present. All the peaks are fitted with Gaussian line shape and centers for the peaks are denoted in nanometers, as shown in Fig. 7. The UV-blue peaks are located at 377 and ~ 400 nm for Ge1; 377, 382, and ~ 400 nm for Ge2; and 343 and ~ 400 nm for Ar1. Since the ~ 400 and ~ 500 nm peaks are common to all samples including Ar1 where no Ge is present, these emission bands cannot be directly related to Ge NCs or Ge related defects, such as GeO_2 . This may be attributed to the defects in the surrounding SiO_x matrix or the defects at the NC/ SiO_x interface. Note that all three samples have a NC/ SiO_2 interface in common, although the nature of the oxide is quite different in different samples due to the different preparation conditions.

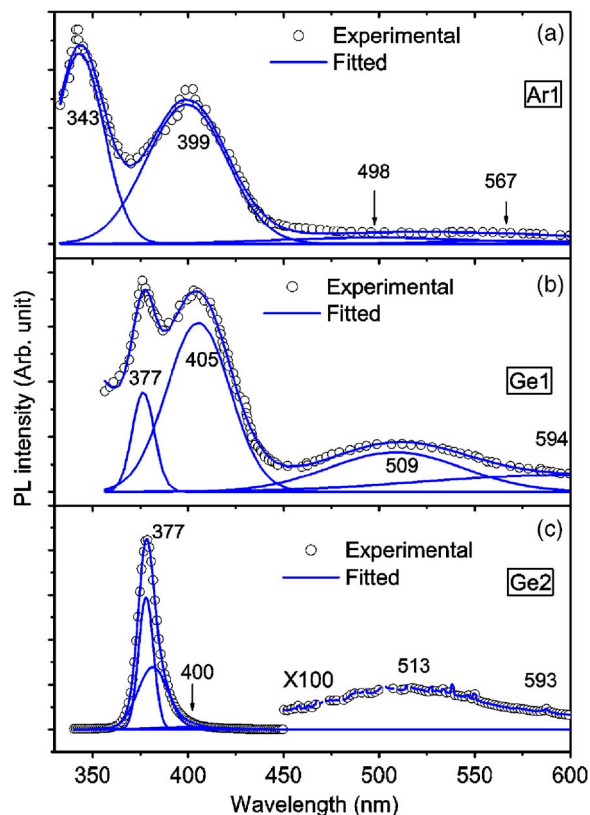


FIG. 7. (Color online) PL spectra of (a) Ar1, (b) Ge1, and (c) Ge2 samples with 325 nm excitation. Multiple peaks are fitted with Gaussian line shapes and center of each peak is denoted with number in nanometers. A weak broad peak around ~ 500 nm and a strong peak at ~ 400 nm are common to all samples. For Ge2 sample, ~ 500 nm band is weak as compared to the ~ 377 nm band; hence a portion of the data is shown with a $100\times$ magnification.

F. PL excitation spectroscopy

In order to understand further the nature of the UV emission band, we performed the PLE spectroscopy by keeping the emission wavelength fixed at 377 nm for Ge1 and Ge2 and at 350 nm for Ar1. Note that the ~ 400 nm PL emission has been observed by several groups and there is some consensus regarding its origin. Therefore, we choose to study more details of the UV bands. Figure 8 shows the PLE spectra that show a broad excitation peak centered at ~ 320 nm for the 377 nm emission from both Ge1 and Ge2 samples. Ar1 shows a similar excitation band at ~ 318 nm for the emission at ~ 350 nm. Thus, all three samples exhibit a very large Stokes shift (>0.5 eV) between the absorption and emission of a specific band. The Stokes shift characterizes the energy relaxation between the excitons that takes place within inhomogeneously broadened absorption line and inhomogeneous broadening may result from interfacial roughness, defects, impurities, and other structural imperfection.³⁹ In the present case, interfacial roughness is quite likely to be present due to the formation of nanoclusters/NCs in the defective oxide matrix. Hence, the observed Stokes shift is a strong indicator of a defective interface between the NC and SiO_2 matrix in all three samples, and the broad UV emission bands are most likely related to the interface defects.

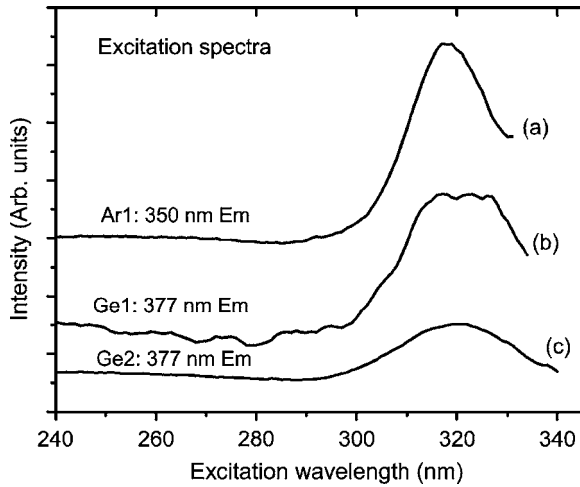


FIG. 8. PLE spectra for (a) Ar1, (b) Ge1, and (c) Ge2. Emission was monitored at a fixed wavelength as indicated for each curve.

G. Time resolved PL studies

A powerful technique to explore dynamical characteristics of the carriers that contribute to the PL is the time resolved PL spectroscopy. Figure 9 shows the PL decay dynamics for the Ge1 and Ge2 samples excited with a 378 nm excitation pulse. The PL emission was monitored for a wavelength above 385 nm, which means the decay dynamics of the ~ 400 and ~ 500 nm bands are monitored in this experiment. Reference data shown with dashed line refer to the system response for the lifetime measurement, which results from the scattering from a standard liquid sample. The reference data were subtracted from the sample data to extract the decay time constant (τ). The resulting decay curves show

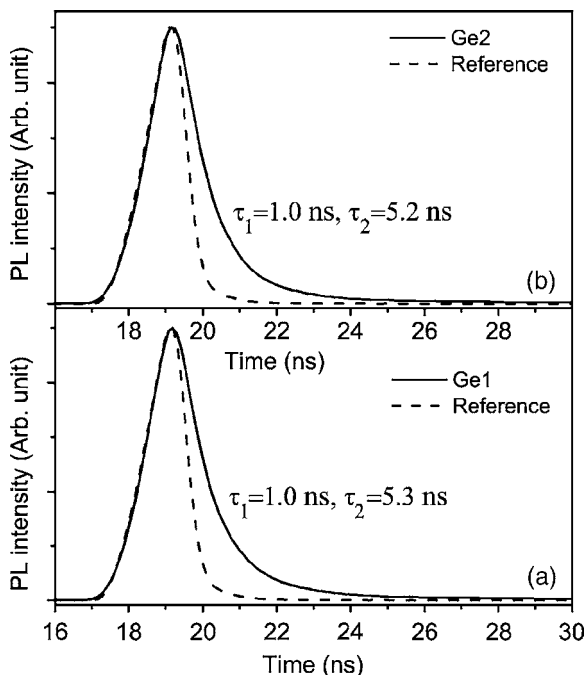


FIG. 9. PL decay dynamics of violet emission from SPT1 and SPT2 samples. After subtracting the reference data, the experimental data could be fitted well with two exponentials with time constants τ_1 and τ_2 . The decay curve is dominated by time constant τ_1 (1.0 ns) in both the samples.

a double exponential dynamics of recombination with time constants $\tau_1=1.0$ ns and $\tau_2=5.3$ ns as obtained from fitting, for both the samples. As the time constants are independent of the size of the Ge NCs present in the samples, the fast decay dynamics is unlikely to originate from the recombination at the core of the NCs. From the fitting parameters, it is found that the amplitude of τ_1 component of decay is nine orders of magnitude higher than the amplitude of τ_2 component. We also performed decay measurement at a fixed emission wavelength of 400 nm using a monochromator and the resulting PL decay data could be fitted (not shown) with a time constant of $\tau_1=1.0$ ns. This decay rate is quite fast as compared to the radiative lifetime predicted for Ge NCs. Niquet *et al.*¹¹ predicted that radiative lifetime for Ge NCs should be long (0.1–1.0 ms) in spite of the small difference between the direct and indirect gaps of bulk Ge. Zacharias and Fauchet observed a nanosecond PL dynamics for the ~ 400 nm band in sputter deposited Ge NCs and the fast response was attributed to defects at the nanocrystal/matrix interface.⁴ We attribute the observed faster decay component ($\tau_1=1.0$ ns) to nonradiative recombination at defects and the slower component ($\tau_2=5.2$ ns) to radiative recombination at the NC/SiO₂ interface defects.

H. Origin of the PL bands

In the literature, ~ 545 nm PL band has been commonly attributed to defects in the SiO₂ matrix, such as nonbridging oxygen hole center, *E* center, etc.^{4,6,40} The peak position of visible PL band in the SiO₂ has been found to depend on the SiO₂ composition.⁴¹ Indeed, Rutherford backscattering studies on Ar1 samples showed that the Ar implanted thermally grown SiO_x layer is oxygen deficient, i.e., it has a composition of $x \approx 1.8$. Similar oxygen deficient SiO₂ layer is also present in sputter deposited samples, since depositions were made with Si and Ge targets in the presence of oxygen discharge.²⁸ Hence, in accordance with the literature reports, we attribute the ~ 545 nm PL band to nonbridging oxygen hole centers in the SiO₂ matrix.

In the literature, the ~ 400 nm blue peak has been assigned to Ge/O related defects in sputter deposited Ge NCs (Ref. 4) or the defects at the interface between Ge NC and SiO₂ matrix.⁴² However, our results indicate that ~ 400 nm emission is not unique to the presence of Ge in the SiO₂, since it is found in Ge-free SiO₂ sample as well. Note that ~ 400 nm band is very intense in both Ge1 and Ar1 as compared to a low intensity peak in Ge2. There are two possible sources for the ~ 400 and ~ 500 nm peaks in our samples. First, since the oxygen deficient defects are common to all samples and the density of these defects reduces with higher annealing temperature/time, oxygen deficient defects in SiO₂ are likely candidate for these strong emission bands. Second, the interface between NCs and surrounding defective matrix changes as a function of annealing temperature and time. A NC/SiO₂ interface is common to all three samples including Ar1, where Si NCs are present as revealed from the LFRS studies. Thus, it is the interface between the NC/SiO₂ matrix that may be responsible for these bands, irrespective of the species of nanocluster. In Ge2 sample, oxide quality is ex-

pected to be improved due to the higher temperature of annealing and we observe very low intensity of the ~ 400 nm peak. The NC/SiO₂ interface is different in various samples (obtained with different processing conditions) and it gives rise to variations in the UV emission bands (343, 377, and 377 nm peaks for Ar1, Ge1, and Ge2 samples, respectively), as observed in Fig. 7. Note that the band gap of nonstoichiometric SiO_x ranges from 1.8 to 4.0 eV and strongly depends on its composition.⁴ In the case of Ar1, the oxide matrix is highly defective as revealed from the FTIR analysis and hence a lower wavelength emission may be expected. Tong *et al.* observed the adjustable UV emission bands from silicon rich oxide films.⁴³ We find that the 377 nm emission band is very strong in Ge2 as compared to that of Ge1, perhaps because of higher density of Ge NCs that form the interface. Kim *et al.*⁴⁴ observed an UV PL band at 365 nm from silicon rich oxide layer and ascribed it to the hole trapped E' center ($O_3 \equiv Si\cdot$). However, E' center was found to completely anneal out in the temperature range of 500–700 °C.^{21,36} Hence, any mechanism related to bulk defects in SiO₂ seems unreasonable for the 343–377 nm bands. In sputter deposited silicon oxide, Song *et al.*²¹ argued that a twofold coordinated Si defect of SiO₂ ($O-\dot{Si}-O$) at the interface between NC Si and the SiO₂ is responsible for the 370 nm PL band. We believe that the UV bands originate from the defects at the NC/SiO₂ interface. This proposition for the UV band is strongly supported by our PLE data, which shows a large Stokes shift. Further, the results of Raman analysis and the PL analysis are consistent, because the presence of substoichiometric Si oxide and defective interface between NCs and surrounding matrix naturally cause inhomogeneous strain in the Ge NCs. The strain field may cause local change of band structure and interface states are primarily responsible for the UV emission.

It is noteworthy that despite the presence of well-formed spherical Ge NCs in the sputter deposited samples and those reported in the literature, the observed visible or UV emission could not be related to radiative recombination of excitons confined in the Ge NCs. Rather all the bands are related to defects in the surrounding matrix and the defects at the interface between NCs and oxide matrix. It is clear from our results that embedded Ge NCs are strained due to the several possible reasons: (i) Lattice mismatch between Ge crystallites and surrounding SiO₂, (ii) poor Ge/SiO₂ interface quality due to the defective oxide matrix as well as lattice mismatch, (iii) possible presence of substoichiometric Ge oxide (GeO_x) in and around the Ge NCs, and (iv) surface reconstruction induced disordering of near surface atoms in Ge NCs. Due to the large atomic mass of Ge, surface reconstruction of Ge NCs may not be perfect under nominal thermal treatment and effectively a disordered structure may result.⁴⁵ Thus, when the Ge NCs are strained, the band structure and electronic density of states would modify as compared to that predicted for unstrained NCs. It is quite likely that these strain induced band gap states act as nonradiative channel and may quench the expected PL from quantum confined carriers. Another possibility is that the photogenerated carriers may prefer to recombine at the interface states and suffi-

cient carriers may not be available for recombination at the core of Ge NCs. Thus, the light emission becomes less efficient for the Ge NCs.

IV. CONCLUSIONS

We have studied the structural and PL properties of Ge NCs embedded in SiO₂ matrix grown by sputter deposition method. The analysis of the optical Raman spectra clearly indicates the presence of strain in the Ge NCs of size 7–8 nm. Polarized low frequency Raman spectra show surface symmetrical (0,0) and surface quadrupolar (0,2) acoustic phonon modes of Ge NCs. PL studies using UV and visible excitations show several strong emission bands in the UV region and a relatively weak and broad visible band. A careful analysis of PL data along with PLE spectra shows that various PL bands originate from oxygen deficient defects in the surrounding SiO₂ matrix and twofold coordinated silicon defects at the NC/SiO₂ interface. It is believed that the strain in the Ge NC and the interface defects are likely to partially quench the expected PL from excitonic recombination at the core of the Ge NCs.

ACKNOWLEDGMENTS

Financial assistance from Board of Research in Nuclear Sciences (BRNS), Department of Atomic Energy (DAE), and University Grants Commission (UGC)-DAE through sponsored projects is gratefully acknowledged.

- ¹K. S. Min, K. V. Shcheglov, C. M. Yang, H. A. Atwater, M. L. Brongersma, and A. Polman, *Appl. Phys. Lett.* **68**, 2511 (1996).
- ²X. L. Wu, T. Gao, G. G. Siu, S. Tong, and X. M. Bao, *Appl. Phys. Lett.* **74**, 2420 (1999).
- ³Y. Maeda, *Phys. Rev. B* **51**, 1658 (1995); Y. Kanemitsu, H. Uto, Y. Masumoto, and Y. Maeda, *Appl. Phys. Lett.* **61**, 2187 (1992).
- ⁴M. Zacharias and P. M. Fauchet, *Appl. Phys. Lett.* **71**, 380 (1997).
- ⁵G. Kartopu, S. C. Bayliss, R. E. Hummel, and Y. Ekinici, *J. Appl. Phys.* **95**, 3466 (2004).
- ⁶L. Rebohle, J. von Borany, R. A. Yankov, W. Skorupa, I. E. Tyschenko, H. Fröb, and K. Leo, *Appl. Phys. Lett.* **71**, 2809 (1997).
- ⁷P. K. Sahoo, S. Dhar, S. Gasiorek, and K. P. Lieb, *J. Appl. Phys.* **96**, 1392 (2004).
- ⁸L. S. Liao, X. M. Bao, X. Q. Zheng, N. S. Li, and N. B. Min, *Appl. Phys. Lett.* **68**, 850 (1996).
- ⁹A. Singha, A. Roy, D. Kabiraj, and D. Kanjilal, *Semicond. Sci. Technol.* **21**, 1691 (2006).
- ¹⁰S. Takeoka, M. Fujii, S. Hayashi, and K. Yamamoto, *Phys. Rev. B* **58**, 7921 (1998).
- ¹¹Y. H. Niquet, G. Allan, C. Delerue, and M. Lannoo, *Appl. Phys. Lett.* **77**, 1182 (2000).
- ¹²X. Ma, W. Shi, and B. Li, *Semicond. Sci. Technol.* **21**, 713 (2006).
- ¹³E. W. H. Kan, W. K. Chim, C. H. Lee, W. K. Choi, and T. H. Ng, *Appl. Phys. Lett.* **85**, 2349 (2004).
- ¹⁴S. Takeoka, M. Fujii, S. Hayashi, and K. Y. Yamamoto, *Appl. Phys. Lett.* **74**, 1558 (1999).
- ¹⁵J. Y. Zhang, Y. H. Ye, X. L. Tan, and X. M. Bao, *J. Appl. Phys.* **86**, 6139 (1999).
- ¹⁶S. H. Choi, S. C. Han, and S. Hwang, *Thin Solid Films* **413**, 177 (2002).
- ¹⁷L. Rebohle, J. von Borany, H. Frob, T. Gebel, M. Helm, and W. Skorupa, *Nucl. Instrum. Methods Phys. Res. B* **188**, 28 (2002).
- ¹⁸F. Meinardi and A. Paleari, *Phys. Rev. B* **58**, 3511 (1998).
- ¹⁹M. Avella, A. C. Prieto, J. Jimenez, A. Rodriguez, J. Sangrador, and T. Rodriguez, *Solid State Commun.* **136**, 224 (2005).
- ²⁰R. Salh, L. Fitting, E. V. Kolesnikova, A. A. Sitnikova, M. V. Zamoryanskaya, B. Schmidt, and H.-J. Fitting, *Semiconductors* **41**, 381 (2007).
- ²¹H. Z. Song, X. M. Bao, N. S. Li, and X. L. Wu, *Appl. Phys. Lett.* **72**, 356 (1998).

- ²²X. Yang, X. L. Wu, S. H. Li, H. Li, T. Qui, Y. M. Yang, P. K. Chu, and G. G. Siu, *Appl. Phys. Lett.* **86**, 201906 (2005).
- ²³X. W. Du, L. Y. Liu, P. Yao, and L. Cui, *J. Appl. Phys.* **100**, 076102 (2006).
- ²⁴X. L. Wu, T. Gao, X. M. Bao, F. Yan, S. S. Jiang, and D. Feng, *J. Appl. Phys.* **82**, 2704 (1997).
- ²⁵W. K. Choi, H. G. Chew, F. Zheng, W. K. Chim, Y. L. Foo, and E. A. Fitzgerald, *Appl. Phys. Lett.* **89**, 113126 (2006).
- ²⁶E. Duval, A. Boukenter, and B. Champagnon, *Phys. Rev. Lett.* **56**, 2052 (1986).
- ²⁷L. Saviot, D. B. Murray, and M. C. M. Lucas, *Phys. Rev. B* **69**, 113402 (2004).
- ²⁸K. Das, M. N. L. Goswami, A. Dhar, B. K. Mathur, and S. K. Ray, *Nanotechnology* **18**, 175301 (2007).
- ²⁹M. I. Alonso and K. Winer, *Phys. Rev. B* **39**, 10056 (1989).
- ³⁰H. Richter, J. P. Wang, and L. Ley, *Solid State Commun.* **39**, 625 (1981); I. H. Campbell and P. M. Fauchet, *ibid.* **58**, 739 (1986).
- ³¹I. D. Sharp, Q. Xu, D. O. Yi, C. W. Yuan, J. W. Beeman, K. M. Yu, J. W. Ager III, D. C. Chrzan, and E. E. Haller, *J. Appl. Phys.* **100**, 114317 (2006).
- ³²J. M. J. Lopes, F. C. Zawislak, M. Behar, P. F. P. Fichtner, L. Rebohle, and W. Skorupa, *J. Appl. Phys.* **94**, 6059 (2003).
- ³³E. Duval, *Phys. Rev. B* **46**, 5795 (1992).
- ³⁴A. Tanaka, S. Onari, and T. Arai, *Phys. Rev. B* **47**, 1237 (1993).
- ³⁵P. K. Giri, R. Kesavamoorthy, S. Bhattacharyya, B. K. Panigrahi, and K. G. M. Nair, *Mater. Sci. Eng., B* **128**, 201 (2006).
- ³⁶M. Fujii, Y. Kanzawa, S. Hayashi, and K. Yamamoto, *Phys. Rev. B* **54**, R8373 (1996).
- ³⁷R. N. Pereira, J. S. Jensen, J. Chevallier, B. B. Nielsen, and A. N. Larsen, *J. Appl. Phys.* **102**, 044309 (2007).
- ³⁸K. Das, M. N. Goswami, R. Mahapatra, G. S. Kar, A. Dhar, H. N. Acharya, S. Maikap, J.-H. Lee, and S. K. Ray, *Appl. Phys. Lett.* **84**, 1386 (2004).
- ³⁹G. D. Gilliland, *Mater. Sci. Eng., R*, **18**, 99 (1997).
- ⁴⁰X. Jie, A. T. S. Wee, C. H. A. Huan, W. X. Sun, Z. X. Shen, and S. J. Chua, *Mater. Sci. Eng., B* **107**, 8 (2004).
- ⁴¹J. Linnros, N. Lalic, A. Galeckas, and V. Grivickas, *J. Appl. Phys.* **86**, 6128 (1999).
- ⁴²M. I. Ortiz, A. Rodríguez, J. Sangrador, T. Rodríguez, M. Avella, J. Jiménez, and C. Ballesteros, *Nanotechnology* **16**, S197 (2005).
- ⁴³J. F. Tong, H. L. Hsiao, and H. L. Hwang, *Appl. Phys. Lett.* **74**, 2316 (1999).
- ⁴⁴K. Kim, M. S. Suh, T. S. Kim, C. J. Youn, E. K. Suh, Y. J. Shin, K. B. Lee, H. J. Lee, M. H. An, H. J. Lee, and H. Ryu, *Appl. Phys. Lett.* **69**, 3908 (1996).
- ⁴⁵I. D. Sharp, Q. Xu, C. Y. Liao, D. O. Yi, J. W. Beeman, Z. Liliental-Weber, K. M. Yu, D. N. Zakharov, J. W. Ager III, D. C. Chrzan, and E. E. Haller, *J. Appl. Phys.* **97**, 124316 (2005).